

Evaluation of Weather Research and Forecast (WRF) microphysics schemes in simulating zenith total delay for InSAR atmospheric correction

Xinyi Wang, Qiming Zeng, Jian Jiao & Zhenhang Hao

To cite this article: Xinyi Wang, Qiming Zeng, Jian Jiao & Zhenhang Hao (2021) Evaluation of Weather Research and Forecast (WRF) microphysics schemes in simulating zenith total delay for InSAR atmospheric correction, International Journal of Remote Sensing, 42:9, 3456-3473, DOI: [10.1080/01431161.2020.1807649](https://doi.org/10.1080/01431161.2020.1807649)

To link to this article: <https://doi.org/10.1080/01431161.2020.1807649>



[View supplementary material](#)



Published online: 11 Feb 2021.



[Submit your article to this journal](#)



Article views: 127



[View related articles](#)



[View Crossmark data](#)



Evaluation of Weather Research and Forecast (WRF) microphysics schemes in simulating zenith total delay for InSAR atmospheric correction

Xinyi Wang^a, Qiming Zeng^a, Jian Jiao^a and Zhenhang Hao^b

^aInstitute of Remote Sensing and Geographic Information System, Peking University, Beijing, China; ^bSchool of Geology and Geomatics, Tianjin Chengjian University, Tianjin, China

ABSTRACT

Many researches have demonstrated the potential of Interferometric Synthetic Aperture Radar (InSAR) atmospheric correction method based on the Weather Research and Forecast (WRF) model. However, there remain some doubts about its robustness and accuracy over complex topographical areas. For meteorology, microphysics schemes play a significant role on the simulation of atmospheric parameters. But no studies have focused specifically on the impact of the microphysics schemes (MPs) on the atmospheric zenith total delay (ZTD) simulation for InSAR atmospheric correction. Therefore, we test four sophisticated MPs in WRF version 3.9.1 to simulate ZTD during the SAR signal propagation over Haiyuan in China in summer. And the ZTD values from WRF are validated by comparing to those obtained from four global position system (GPS) stations. The results show that all of the MPs can effectively reconstruct the major absolute ZTD, but regarding differential ZTD values, the Morrison double moment (M2M) and WRF Double moment 6 classes Model (WDM6) predict more accurate differential ZTD data. Moreover, WRF-based InSAR atmospheric correction utilizing the M2M obtains the most accurate deformation map results. A proper choice of MP schemes can enhance the WRF model to simulate more precise ZTD and contribute to reach a conclusion on the robustness of WRF-based InSAR atmospheric correction, especially in the complex mountain area in summer.

ARTICLE HISTORY

Received 30 December 2018
Accepted 1 June 2020

1. Introduction

The atmosphere, particularly tropospheric water vapour, is one of the major sources of error in Synthetic Aperture Radar (SAR) signal propagation (Hanssen et al., 2001). In efforts to remove these effects, many scholars have applied the high-resolution mesoscale numerical forecast model (i.e., Weather Research and Forecast, WRF) to simulate precipitable water vapour (PWV). This method has been analysed by many scholars (Liu, Hanssen, and Mika 2009; Nico et al. 2011; Mateus et al. 2013a; Jung, Kim, and Park 2014; Yun, Zeng et al. 2015; Gong et al. 2015; Bekaert et al. 2015); Some have shown its

CONTACT Qiming Zeng  qmzeng@pku.edu.cn  Institute of Remote Sensing and Geographic Information System, Peking University, Beijing, China

 Supplemental data for this article can be accessed [here](#).

© 2021 Informa UK Limited, trading as Taylor & Francis Group



potential for simulating PWV (Nico et al. 2011; Mateus et al., 2013b) and mitigating environmental effects on Differential Interferometric SAR (D-InSAR) (Jung, Kim, and Park 2014; Yun 2015; Yun, Zeng et al. 2015). However, some have debated these conclusions (Gong et al. 2015; Liu et al., 2009; Bekaert et al. 2015), arguing that WRF is not robust enough to reproduce the atmospheric phase delay, particularly over complex topography in the summer.

However, none of those scholars mentioned the setup of the convective parameterization schemes (i.e., Microphysics schemes (MPs)) in the WRF model except for Yun et al. (2015). Yun et al. determined that selection of the MPs did not directly affect the atmospheric corrections in their case study because there is no substantial reported precipitation from moist processes in their study domain during either simulation period. Hence, in all of the domains, atmospheric water vapour, liquid water, and ice, were handled by the WRF single moment 3 classes (WSM3) microphysics scheme. Nico et al. (Nico et al. 2011) used WRF with the WSM3 simple ice scheme and the Kain-Fritsch (KF) convection scheme. They concluded that the main difference is in a region along the Tagus River and the surrounding mountains, where the capability of the WRF forecasts to reproduce the correct atmospheric parameters is poor due to an unstable fluvial environment cast into a moderately high-relief area. Mateus et al. (Mateus, Nico et al. 2013b) concluded that on a certain day (21 June 2009), the WRF model did not accurately model the atmospheric parameters, without a clear clarification of detailed microphysics they chose. In that study, the mean differences and root-mean-square (RMS) in the summer (June, July, and August) are much larger than they are in the other seasons. However, there is no published research on improving the accuracy of the zenith total delay (ZTD) for InSAR atmospheric correction by choosing more appropriate MP schemes.

For meteorology, it has been a long-standing challenge for mesoscale numerical model to accurately predict the water precipitation events; this is due to the complexities and uncertainties of the precipitation processes involved, such as cumulus convection, micro-physics, and boundary layer parameterization schemes (Shi et al., 2013). However, the MP schemes directly influence the simulation of atmospheric parameters. (Shi 2013; Kan et al., 2016; Kan et al. 2016). To evaluate the effects of these convective schemes on heavy rainfall predictions over Yangtze River valley (YRV) region, Kan et al. (2016) concluded that changes in microphysical parameters greatly influenced the simulated precipitation area. WSM 5 classes (WSM5) simulated best precipitation locations but overestimated the rainfall intensity, while WSM 6 classes (WSM6) predicted the closest rainfall intensity with the realistic observation. Jankov et al. (2005) demonstrated that changes in convective treatment notably impacted the forecast of system average rain rate, while forecasts of total domain rain volume were influenced by choices of microphysics and convective treatment. However, the convective cumulus parametrization is for sub-grid scale cumulus clouds while the microphysics scheme is for resolvable to 'large scale' clouds and precipitation. SAR images cover large areas and so the latter is to be tested in this paper. Besides, the fact is that both calculation of the precipitation prediction and water vapour based on specific humidity or the water vapour mix ratio, which can be simulated by the WRF model. Therefore, MP schemes have the same effect on the simulation of water vapour as the precipitation. Hence, we deduce that the WRF model could not accurately model the atmospheric zenith delay in summer over complicated mountains because inappropriate microphysics schemes were selected.

Here, we first assessed influences of the MP schemes on the atmospheric ZTD simulations of the WRF model and analysed its performance for correcting atmospheric effects. WRF with four different MPs (see [Section 2](#)) is used to forecast three-dimensional fields of temperature, atmospheric pressure, water vapour mixing ratio, and geopotential height at the acquisition times of the SAR images. These quantities are then used to compute the hydrostatic and wet components and to estimate the atmospheric ZTD values. We give constructive suggestions for the WRF model setup in the hope of obtaining more accurate ZTD. This is accomplished by examining which microphysics scheme is better at predicting the ZTD for InSAR atmospheric correction in summer over Haiyuan Mountain.

The remainder of this paper is structured as follows. [Section 2](#) introduces the MP schemes and methods for the evaluation of ZTD obtained from WRF and [global position system \(GPS\)](#) and the principle of InSAR atmospheric correction. [Section 3](#) describes the datasets and WRF model setup. In [Section 4](#), results and discussion are presented. [Section 5](#) contains our conclusions.

2. Schemes and method

The high-resolution mesoscale model WRF (Version 3.9.1) is developed at National Centre for Atmospheric Research (NCAR) in collaboration with other research institutes/universities. It is a mesoscale weather modelling system with flexible resolution and parameterization schemes (Skamarock et al. 2008). The microphysics schemes currently include Kessler Eta Ferrier, Lin et al., WSM3, WSM5, WSM6, Ferrier, Thompson, Morrison double moment (M2M), WRF Double Moment 5 classes scheme (WDM5) and WDM 6 classes scheme (WDM6). We used WSM6 because past research (Kan et al. 2016) suggested that WSM6 scheme could produce better results as it contains more comprehensive processes than other schemes. Meanwhile, we chose the WSM3 scheme because it is used in other similar studies (Yun et al., 2015; Nico et al. 2011) and because, being a relatively simple scheme, it can be used to assess the difference with other more complex schemes. The double moment approaches are considered to be more flexible in representing the water vapour and hydrometeors distributions. Hence, this paper uses the M2M scheme and WDM6 for further simulation and analysis. Overall, four different MP schemes have been utilized to simulate the corresponding parameters and obtain the zenith wet delay (ZWD) and the hydrostatic delay (ZHD) for InSAR atmospheric correction. The details of the different schemes are as follows.

2.1. Microphysics (MPs)

A microphysics scheme has an important effect on the convective process and the computation of the water vapour or ZTD by modulating the structure of temperature and humidity fields and the release of latent heat due to the phase transition of water vapour. We utilize four MPs and outline them below.

2.1.1. WSM3 scheme

The WSM3 microphysics scheme includes ice sedimentation and other new ice-phase parameterizations. This scheme is the default scheme in WRF and computationally



efficient for the inclusion of ice processes but does not consider super-cooled water and gradual melting rates (Hong, Dudhia, and Chen 2004).

2.1.2. WSM6 scheme

In this scheme (Hong and Lim, 2006), a method for representing mixed-phase particle fall speeds for the snow and graupel is implemented by assigning a single fall speed to both that is weighed by the mixing ratios and applying that fall speed to both sedimentation and accumulation processes. Of the three WSM schemes, the WSM6 scheme is the most suitable for cloud resolving grids, considering the efficiency and theoretical background (Mielikainen, Huang, and Huang et al. 2012; Hong, Juang, and Zhao 1998; Hu, Tao, and Zheng et al. 2014).

2.1.3. M2M scheme

This double moment cloud microphysics scheme is based on the parameterization of Morrison, Thompson, and Tatarki (2009). The mixing ratio and number concentration of graupel are added as prognostic variables. Compared with one moment scheme, this scheme can investigate the formation and evolution of trailing stratiform precipitation in an idealized two-dimensional squall line. Also, it predicts both the mixing ratios and number concentrations of at least some hydrometers, while single moment schemes only predict the mixing ratio, thus they must assume a particle size distribution, which causes them less flexible and inappropriate for complex topography compared to the two moment schemes. For the simulation of the atmospheric stratification component, we deduce that it is more suitable than other options.

2.1.4. WDM6 scheme

The WDM6 microphysics scheme has double moment rain. Cloud and Cloud Condensation Nuclei (CCN) for warm process, but is otherwise like WSM6. As the other two moment scheme we chose, WDM6 is more flexible than WSM6 and used to better evaluate the effect of the two moment process on the simulation of atmospheric parameters.

2.2. Evaluation of ZTD and InSAR atmospheric correction

The atmospheric refractivity, described by Equation (1), can be divided into four components and can be calculated in terms of atmospheric parameters: (Hanssen, 2001, 202)

$$N = k_1 \frac{P}{T} + \left(k'_2 \frac{e}{T} + k_3 \frac{e}{T^2} \right) - 4.03 \times 10^7 \frac{n_e}{f^2} + 1.4W \quad (1)$$

where N is the total atmospheric refractivity, P is the partial pressure of dry air in hPa, e is the partial pressure of water vapour in hPa, and T is the absolute temperature in Kelvin. n_e is the electronic number density per cubic metre, and f is the radar frequency. W represents the liquid water content in grams per cubic metre. The constant values are $k_1 = 77.6 \text{ KhPa}^{-1}$, $k'_2 = 23.3 \text{ KhPa}^{-1}$, and $k_3 = 375000 \text{ K}^2 \text{ hPa}^{-1}$. The first component, referred to as the hydrostatic term, is determined by temperature and dry air pressure. The following two terms (in brackets) are the wet terms, which are related to atmospheric PWV. The third term represents the effects of the ionosphere. The fourth term describes

the liquid water component. Then, the atmospheric phase delay effects in interferograms can be calculated using formula (2) (Hanssen Ramon 2001, 202):

$$\Delta L_d = \frac{1}{10^6 \cos(\theta_{inc})} \int_0^H N dh = \Delta L_d^{\text{hydro}} + \Delta L_d^{\text{wet}} + \Delta L_d^{\text{liquid}} + \Delta L_d^{\text{iono}} \quad (2)$$

where ΔL_d is the total atmospheric delay, θ_{inc} is the incidence angle of the radar satellite, and $\Delta L_d^{\text{hydro}}$, ΔL_d^{wet} , $\Delta L_d^{\text{liquid}}$ and ΔL_d^{iono} are the hydrostatic delay, the wet delay, the liquid delay, and the ionospheric delay, respectively. Since the liquid water delay term reaches only a few mm in the atmospheric phase delay effect, it can be neglected in the computation of the total atmospheric phase delay effect. The ionospheric delay can also be ignored because the spatial variation of total electrons in mid-latitude area is not severe, especially for the band C. Therefore, Equation (2) can be approximated as the following: (Jung, Kim, and Park 2014).

$$\Delta L_d \approx \Delta L_d^{\text{hydro}} + \Delta L_d^{\text{wet}} \quad (3)$$

Hydrostatic delay and wet delay are then computed using Equations (4) and (5) by employing meteorological parameters (i.e. pressure, temperature, and water vapour mixing ratio) extracted from the WRF model (Yun 2015):

$$\Delta L_d^{\text{wet}} = \frac{1}{\cos(\theta_{inc})} \times \Pi^{-1} \times \frac{1}{\rho_{\text{water}}} \sum_{k=0}^N \frac{P_k}{R_q T_v^k} Q_{\text{vapour}}^k \Delta z \quad (4)$$

where Π^{-1} is the unitless proportionality constant and generally ranges from 6.0 to 6.5 (Bevis et al. 1992; Li et al., 2005; Mateus, Nico, and Miranda 2013b), here we use 6.4 for simplicity (Mateus, Nico, and Miranda 2013b). ρ_{water} is the water density, k is the vertical layer, N is the maximum number of vertical layers set in the parameter schemes, and $R_d = 287.0583 \text{ J K}^{-1} \text{ kg}^{-1}$. P_k is the atmospheric pressure, T_v^k is the virtual temperature, Q_{vapour}^k is the mixing ratio of water vapour, and Δz is the total geopotential height in the vertical k th layer.

$$\Delta L_d^{\text{hydro}} = \frac{1}{\cos(\theta_{inc})} \times 2.2779 \times \frac{P_s}{1 - 0.00266 \cos 2\theta - 0.00028 H} \quad (5)$$

where P_s is the measured total surface pressure in millibars, θ is the latitude in degrees, and H is the surface height in metres (Davis et al., 1985; Elgered 1991). The ZTD consists of zenith wet delay (ΔL_d^{wet}) and zenith hydrostatic delay ($\Delta L_d^{\text{hydro}}$) in the tropospheric atmosphere.

2.3. InSAR atmospheric correction

The phase derived from interferometric two repeat-pass SAR images includes the five phase components in Equation (6) (Yun 2015):

$$\varphi_{\text{InSAR}} = \varphi_{\text{orbit}} + \varphi_{\text{topo}} + \varphi_{\text{def}} + \varphi_{\text{atmo}} + \varphi_{\text{noise}} \quad (6)$$

where φ_{InSAR} is the differential interferometric phase between two acquisition times, φ_{orbit} is the phase resulting from the curved geometry of Earth that is eliminated by



using the precise orbit data, φ_{topo} is the topographic phase which can be removed by subtracting a topographic phase simulated from a digital elevation model (DEM), and φ_{noise} is the phase noise resulting from the decorrelation of the InSAR signal due to vegetation coverage or changes in the surface environment which can be eliminated by filtering, φ_{def} is the phase caused by surface deformation along the line-of-sight direction, and φ_{atmo} is the phase contribution of the atmosphere. After conventional D-InSAR processing using the software Generic Mapping Tools SAR (GMTSAR), only the surface deformation term φ_{def} and the atmospheric contribution term φ_{atmo} are left on the right side of [Equation \(6\)](#).

The atmospheric phase delay is calculated by [equation \(7\)](#).

$$\varphi_{\text{atmo}} = \frac{4\pi}{\lambda} \times (\Delta L_d^m - \Delta L_d^s) \quad (7)$$

where λ is the wavelength of satellites. ΔL_d^m , ΔL_d^s Represent the atmospheric delay at the acquisition time of the master image and slave image, respectively.

The atmospheric phase delay is then subtracted from the unwrapped interferograms to mitigate the atmospheric effects (see [equation \(8\)](#)).

$$\varphi_{\text{def}} = \varphi_{\text{InSAR}} - \varphi_{\text{atmo}} \quad (8)$$

3. Datasets and experimental design

3.1. Datasets

The Haiyuan area, located in the western part of China, is characterized by large variability of precipitation in summer because of its high and complex topography and its continental monsoon climate (see [Figure 1](#)). Haiyuan Mountain is located in a topographically complex region dominated by diverse steep foothills. Atmospheric flow is strongly affected by this landscape fragmentation.

The interferograms used in this paper were generated using 12 Sentinel-1A SAR images acquired on 7 June and 19 June 2017, on 13 July and 25 July 2017, on 6 August and 18 August 2017, on 14 June and 26 June 2018, on 8 July and 20 July 2018 and on 1 August and 13 August 2018, respectively. The GPS data which are used to assess the experiment are derived from 4 GPS stations that belong to the crustal movement observation network of China (the stars in [Figure 1](#)).

3.2. WRF Model description

In this research, the simulations included 30 sigma levels reaching from the Earth's surface to the model's top at 50 hPa. The spatial configuration of the experiments consisted of three two-way interacting nested domains (shown in [Figure 2](#)) with horizontal resolutions of 9 km (d01), 3 km (d02), and 1 km (d03). Two-way nesting involves feedback from the finer domain to the coarse domain and vice versa.

For this simulation, sensitive experiments were conducted by using four different MPs (WSM3, WSM6, M2M, and WDM6); the other parameterization options are shown in [Table 1](#). GFS dataset with 0.25° resolution and time steps at a 3 hourly interval (<https://rda.ucar.edu/>

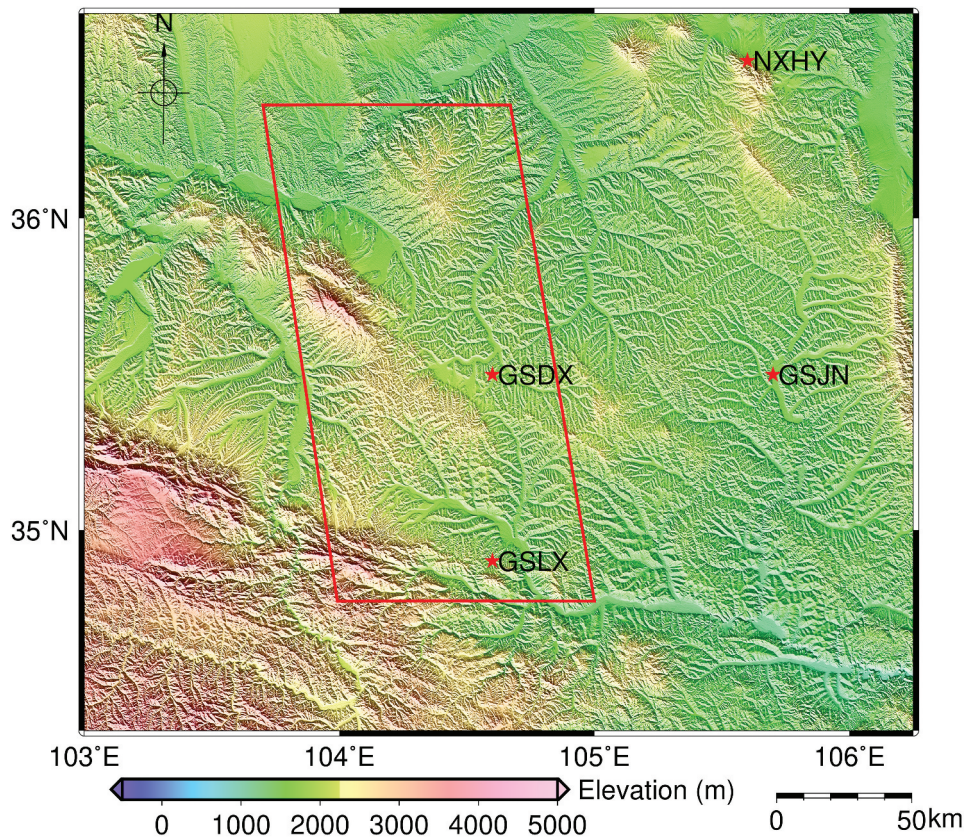


Figure 1. Topographic map of the study area. The red stars represent the 4 continuous GPS stations used in this study and the red rectangle shows the area covered by the SAR images.

[edu/datasets/ds084.1/index.html#sfsl-wl-/data/ds084.1](http://www.esrl.noaa.gov/psd/datasets/ds084.1/index.html#sfsl-wl-/data/ds084.1), from the National Centre for Environment Prediction (NCEP, 2015) are used as initial and boundary conditions. The integration time step for d01 is 54 seconds, and the spin-up period is the first 6 hours.

4. Results and discussion

4.1. Validation of ZTD obtained from WRF with GPS

Accurate knowledge of the atmospheric phase delay is essential for evaluating its potential for correcting atmospheric effects in the realm of differential SAR interferometry. After we completed the calculation of the WRF-ZTDs, we validated them by comparing them with the GPS-ZTDs. Table 2 and Table 3 show the differences between the GPS-ZTD observed at four GPS stations and WRF-ZTD simulated with different MP schemes on 13 July 2017 and 25 July 2017, respectively. Table 4 and Table 5 show the same quantities for 8 July 2018 and 20 July 2018. All of the absolute ZTD values simulated with WRF using different MP schemes are close to the GPS-ZTD values with a maximum difference 19 mm. Among all of the W-G values, M2M shows the minimum ZTD deviation from the reference GPS-ZTD values, followed by the WDM6 scheme. To clearly indicate the differences and

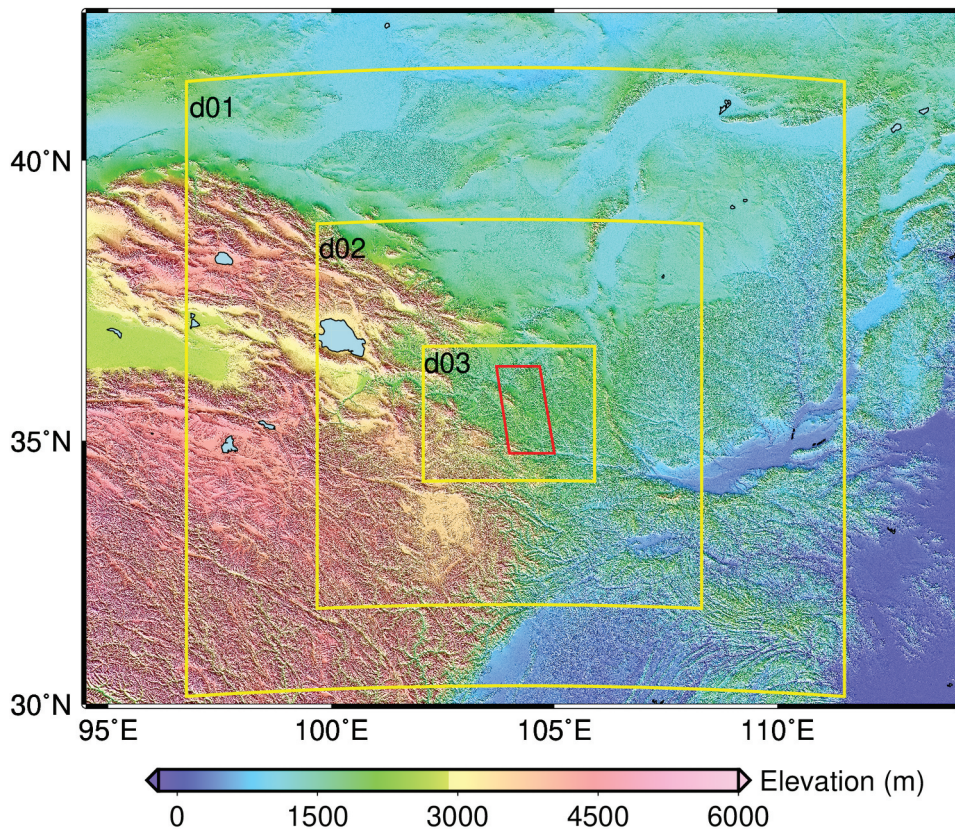


Figure 2. Three two-way interacting nested domains. The d01 domain is the outermost layer and its horizontal resolution is 9 km, d02 is the second domain with 3 km resolution and d03 is the third domain with 1 km resolution. This study uses the d03 domain to assess the simulated atmospheric ZTD and remove the atmospheric effect on the InSAR in the red rectangle.

confirm this result, we calculate the mean absolute error (MAE) of all of the difference for each scheme in the four tables and plot them in [Figure 3](#). The MAE of ZTD deviation simulated from WRF using M2M scheme is the smallest, 3.3 mm, followed by WDM6, 5.8 mm.

For InSAR processes, the differential results of the atmospheric water vapour are required on two different days because the SAR interferograms depend on the two SAR images. Therefore, we calculated the differential ZTD values between 13 July 2017 and 25 July 2017 shown in [Table 6](#) and those between 8 July 2018 and 20 July 2018 shown in [Table 7](#). Concerning the differential values (see [Table 6](#) and [Table 7](#)) corresponding to the InSAR interferograms, the M2M scheme most realistically predicts the differential ZTD.

4.2. WRF-based atmospheric correction for D-InSAR

In this study, the SAR images are processed with GMTSAR software using the two passes differential InSAR approach. Precise orbit data provided by the European Space Agency (ESA) are used to reduce baseline errors, assist with image coregistration, and remove the

Table 1. Parameters chosen in the WRF model for the simulation.

Model component	Parameter chosen
Model domain	Non-hydrostatic
Centre of the domain($^{\circ}$ N, $^{\circ}$ E)	35.5, 104.0
Map projection	Mercator
Horizontal grid system	Arakawa C grid
Integration time step (s)	54
Vertical coordinates	Terrain-following hydrostatic pressure vertical coordinate system with 30 vertical levels
Time integration scheme	3rd order Runge-Kutta Scheme
Advection scheme	6th order centre differencing
Radiation schemes	RRTMG for long wave/RRTMG for shortwave
Surface layer parameterization	Noah land surface model
Planetary boundary layer physics	Yonsei University boundary layer scheme (YSU)
microphysics (MP) schemes	WSM3 + WSM6 + M2M + WDM6
Cumulus (CP) scheme	Grell-Freitas (GF) scheme

Table 2. Absolute ZTD values of GPS and WRF and the difference between them on 13 July 2017. W-G means that GPS-ZTD is subtracted from WRF-ZTD. All values are in mm.

Station	GPS	WSM3	W-G	WSM6	W-G	M2M	W-G	WDM6	W-G
GSDX	1935.7	1927.8	-7.9	1926	-9.7	1931.9	-3.8	1930.3	-5.4
GSJN	2015.0	2031.2	16.2	2024.1	9.1	2015.8	0.8	2012.8	-2.2
GSLX	1943.2	1939.7	-3.5	1938.7	-4.5	1940.7	-2.5	1939.4	-3.8
NXHY	1890.3	1881.9	-8.4	1884.2	-6.1	1889.9	-0.4	1888.0	-2.3

Table 3. Absolute ZTD values of GPS and WRF and the difference between them on 25 July 2017. W-G means that GPS-ZTD is subtracted from WRF-ZTD. All values are in mm.

Station	GPS	WSM3	W-G	WSM6	W-G	M2M	W-G	WDM6	W-G
GSDX	1991.2	1989.2	-2.0	1987.4	-3.8	1990.2	-1.0	1990.0	-1.2
GSJN	2100.0	2092.1	-7.9	2091.0	-9.0	2102.8	2.8	2094.5	-5.5
GSLX	2005.1	2014.6	9.5	2017.8	12.7	2003.0	-2.1	2000.0	-5.1
NXHY	1952.4	1971.4	19.0	1970.9	18.5	1953.7	1.3	1949.1	-3.3

Table 4. Absolute ZTD values of GPS and WRF and the difference between them on 8 July 2018. W-G means that GPS-ZTD is subtracted from WRF-ZTD. All values are in mm.

Station	GPS	WSM3	W-G	WSM6	W-G	M2M	W-G	WDM6	W-G
GSDX	2054.5	2049.3	-5.2	2049.1	-5.4	2051.3	-3.2	2049.8	-4.7
GSJN	2121.7	2113.7	-8.0	2111.7	-10.0	2115.0	-6.7	2112.4	-9.3
GSLX	2117.7	2125.0	7.3	2123.4	5.7	2119.8	2.1	2123.6	5.9
NXHY	2040.5	2025.8	-14.7	2026.6	-13.9	2037.5	-3.0	2037.5	-3.0

Table 5. Absolute ZTD values of GPS and WRF and the difference between them on 20 July 2018. W-G means that GPS-ZTD is subtracted from WRF-ZTD. All values are in mm.

Station	GPS	WSM3	W-G	WSM6	W-G	M2M	W-G	WDM6	W-G
GSDX	2073.7	2081.8	8.1	2083.8	10.1	2074.7	1.0	2075.9	2.2
GSJN	2134.2	2146.2	12.0	2142.0	7.8	2138.0	3.8	2141.0	6.8
GSLX	2130.5	2148.6	18.1	2147.0	16.5	2141.3	10.8	2148.1	17.6
NXHY	2089.7	2078.3	-11.5	2076.0	-13.7	2081.8	-7.9	2080.4	-9.3

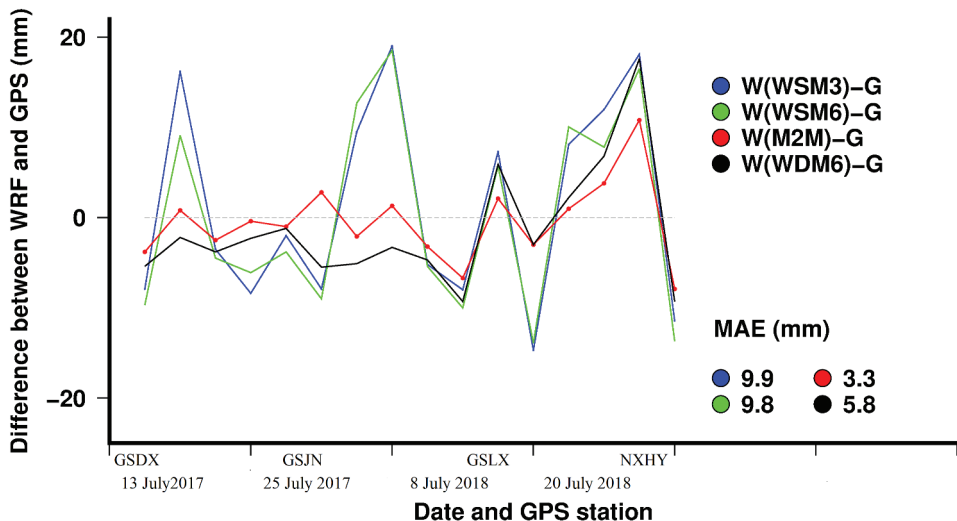


Figure 3. Difference of WRF-ZTD using four different MP schemes minus GPS-ZTD in the different GPS stations (GSDX, GSJN, GSLX, NXHY) on the 13 July 2017, 25 July 2017, 8 July 2018 and 20 July 2018, respectively.

Table 6. Differential ZTD values (Table 2 data minus Table 3 data) and the difference between WRF-ZTD and GPS-ZTD. W-G means that differential GPS-ZTD is subtracted from WRF-ZTD. All values are in mm.

Station	GPS	WSM3	W-G	WSM6	W-G	M2M	W-G	WDM6	W-G
GSDX	-55.5	-61.4	-5.9	-61.4	-5.9	-58.3	-2.8	-59.7	-4.2
GSJN	-85.0	-60.9	24.1	-66.9	18.1	-87.0	-2.0	-81.7	3.3
GSLX	-61.9	-74.9	-13.0	-79.1	-17.2	-62.3	-0.4	-60.6	1.3
NXHY	-62.1	-89.5	-27.4	-86.7	-24.6	-63.8	-1.7	-61.1	1.0

Table 7. Differential ZTD values (Table 4 data minus Table 5 data) and the difference between WRF-ZTD and GPS-ZTD. W-G means that differential GPS-ZTD is subtracted from WRF-ZTD. All values are in mm.

Station	GPS	WSM3	W-G	WSM6	W-G	M2M	W-G	WDM6	W-G
GSDX	-19.2	-32.5	-13.3	-34.7	-15.5	-23.4	-4.2	-26.1	-6.9
GSJN	-12.5	-32.5	-20.0	-30.3	-17.8	-23.0	-10.5	-28.6	-16.1
GSLX	-12.8	-23.6	-10.8	-23.6	-10.8	-21.5	-8.7	-24.5	-11.7
NXHY	-49.2	-52.5	-3.3	-49.4	-0.2	-44.3	4.9	-42.9	6.3

flat earth phase of Sentinel-1A SAR interferometric pairs. A digital elevation model (DEM) with nominal 90 m sample spacing provided by the National Aeronautics and Space Administration (NASA) Shuttle Radar Topography Mission (SRTM) is employed to simulate the height map in the radar coordinate system and to mitigate the topographic phase in the InSAR interferograms. Using the ZTD simulated from the WRF model, atmospheric effects are removed from the InSAR interferograms. Considering that the temporal baseline is 12 days and that no significant seismic activity occurred during this time interval, we consider deformation to be more accurate if the surface map results are close to 0 mm.

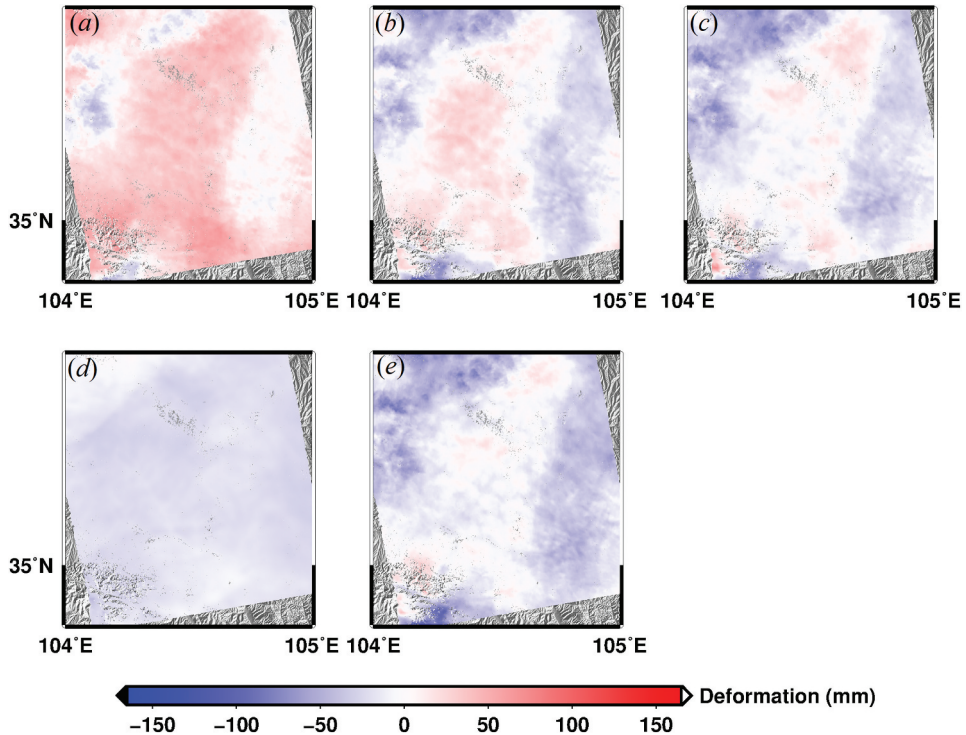


Figure 4. Deformation maps of 13 July and 25 July 2017 obtained from uncorrected interferograms and from interferograms corrected with WRF using different MP schemes. (a) Uncorrected, (b) WSM3, (c) WSM6, (d) M2M, (e) WDM6.

Figure 4 and Figure 5 indicate the deformation maps obtained from D-InSAR with and without WRF-based atmospheric correction utilizing different MPs for on 13 July 2017 and 25 July 2017 and on 8 July 2018 and 20 July 2018, respectively. Table 8 and Table 9 present the mean, standard deviation (STD) and RMS of the deformation maps in Figure 4. Quantitatively, all the schemes mitigate the atmospheric effect to some different extents. Note that the M2M scheme considerably reduced the RMS and STD compared with other schemes. The application of the WRF-based atmospheric correction using the M2M scheme yields the greatest decrease of the mean, STD, and RMS of the deformation maps relative to the uncorrected case, both for 13 July 2017 and 25 July 2017 and on 8 July 2018 and 20 July 2018 (see the last lines in Table 8 and Table 9). As double moment MP schemes are higher complexity and more comprehensive, we conceive that M2M predicts more accurately the atmospheric wet component, which accounts for most of the total delay, compared to single moment microphysics schemes (i.e., WSM3 and WSM6). The WSM3 does not seem particularly good at correcting the atmospheric effects in the deformation map.

To take those steps further, according to the conclusion above that M2M scheme produces the most precise absolute ZTD data and differential ZTD values, we conducted more experiments utilizing the M2M scheme for four other InSAR interferograms in June, August 2017 and June, August 2018 to validate the applicability of microphysics schemes in summer. The absolute GPS-ZTD and WRF-ZTD values are calculated to make the

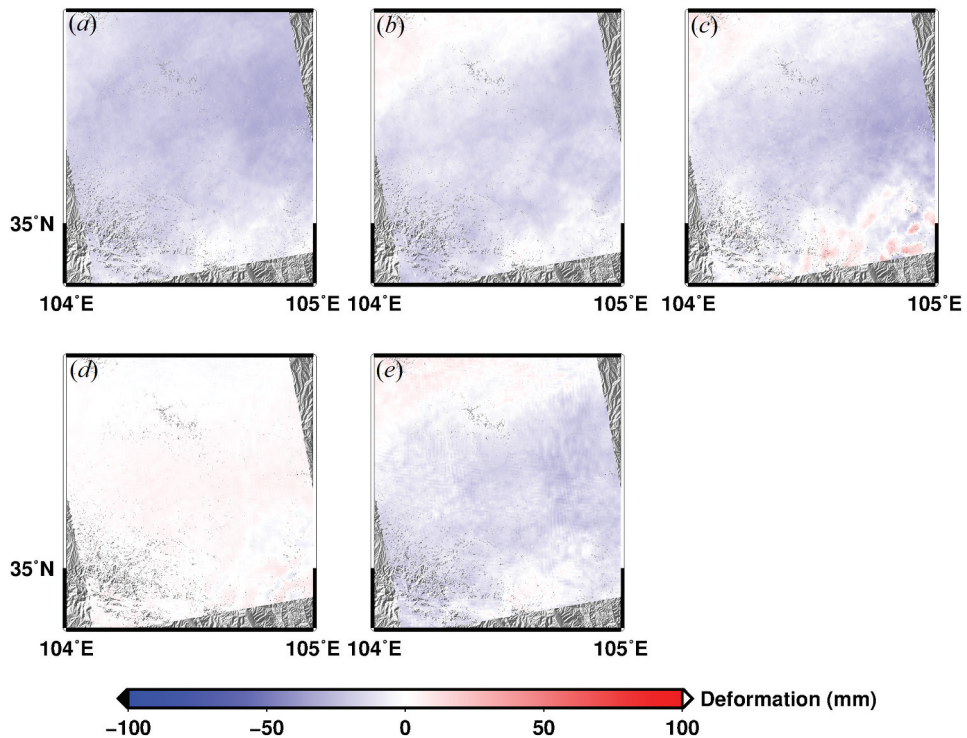


Figure 5. Deformation maps of 8 July and 20 July 2018 obtained from uncorrected interferograms and from interferograms corrected with WRF using different MP schemes. (a) Uncorrected, (b) WSM3, (c) WSM6, (d) M2M, (e) WDM6.

Table 8. Mean, STD and RMS of the deformation maps computed from D-InSAR of 13 July 2017 and 25 July 2017 for the uncorrected case and for six cases with the WRF-based atmospheric correction (AC).

AC or not	MP	Mean (mm)	STD (mm)	RMS (mm)
Uncorrected		16.3	20.3	26.0
WRF-based AC	WSM3	-13.5	12.1	14.6
WRF-based AC	WSM6	-2.7	10.3	10.7
WRF-based AC	M2M	-2.7	4.3	4.6
WRF-based AC	WDM6	-6.3	7.4	8.6

Table 9. Mean, STD and RMS of the deformation maps computed from D-InSAR of 8 July 2018 and 20 July 2018 for the uncorrected case and for six cases with the WRF-based atmospheric correction (AC).

AC or not	MP	Mean (mm)	STD (mm)	RMS (mm)
Uncorrected		-17.2	10.3	20.0
WRF-based AC	WSM3	-12.7	13.3	18.4
WRF-based AC	WSM6	-9.0	12.3	15.1
WRF-based AC	M2M	-3.0	4.1	5.2
WRF-based AC	WDM6	-5.5	7.5	8.4

conclusion more convincing, but shown in the supplemental material S1 to avoid the main body too long and the W-G values are plotted in Figure 6. The differential GPS-ZTD

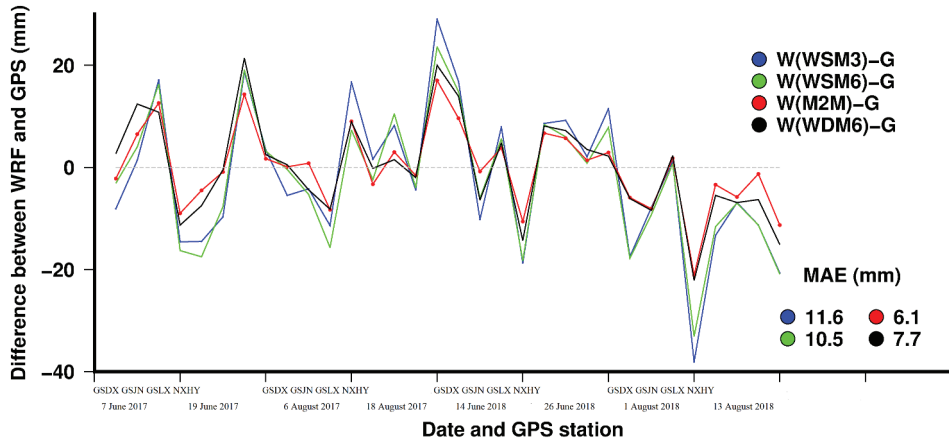


Figure 6. Difference of WRF-ZTD using four different MPs minus GPS-ZTD in the different GPS stations (GSDX, GSJN, GSLX, NXHY) on the 7 June 2017, 19 June 2017, 6 August 2017, 18 August 2017, 14 June 2018, 26 June 2018, 1 August 2018 and 13 August 2018, respectively.

and WRF-ZTD values are shown in the supplemental material S2 and the difference of the differential WRF-ZTD subtracting differential GPS-ZTD values is shown in Figure 7.

Figures 6 and Figure 7 show that all of the MPs can closely reproduce the absolute ZTD values and differential ZTD data compared to the GPS-ZTDs, respectively. Note that M2M still produces the closest ZTD values than the other three schemes. Figure 8, Figure 9, Figure 10, and Figure 11 show the InSAR deformation results with and without WRF-based atmospheric correction using the M2M and WSM3 and Table 10 indicates the MAE, STD, and RMS of the deformation maps. WRF-based atmospheric correction using the M2M significantly removes the atmospheric impact, similarly to what already obtained for the cases of July 2017 and 2018.

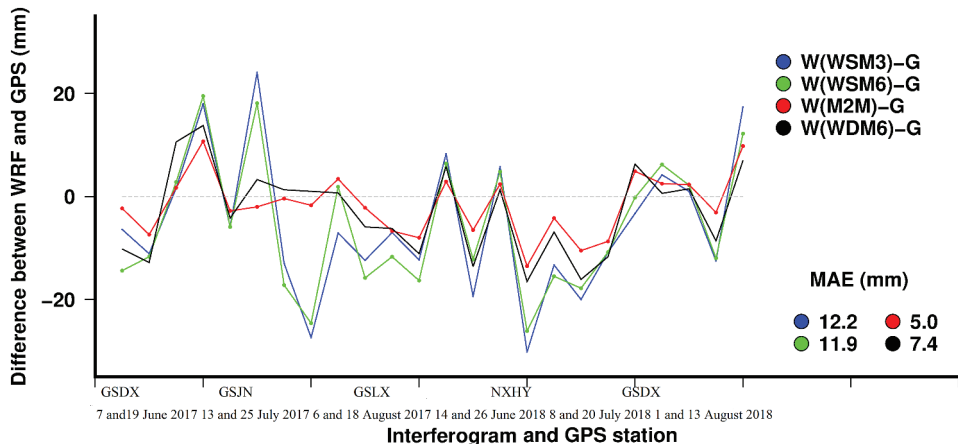


Figure 7. Difference of differential WRF-ZTD using four different MPs minus the differential GPS-ZTD values in the different GPS stations on the 7 and 19 June 2017, 13 and 25 July 2017, 6 and 18 August 2017, 14 and 26 June 2018, 8 and 20 July 2018, 1 and 13 August 2018, respectively.

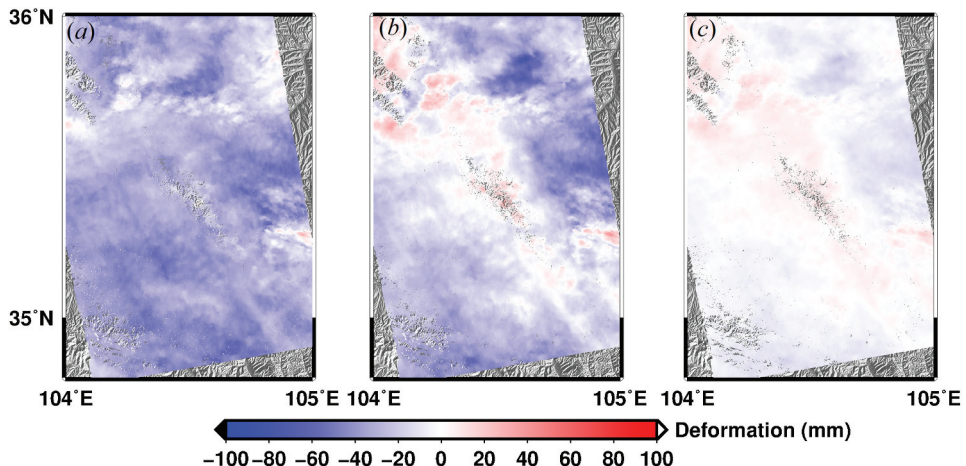


Figure 8. Comparison of uncorrected deformation map with deformation maps corrected with WRF using two different MPs for the dates 7 June and 19 June 2017. (a) Uncorrected, (b) WSM3, (c) M2M.

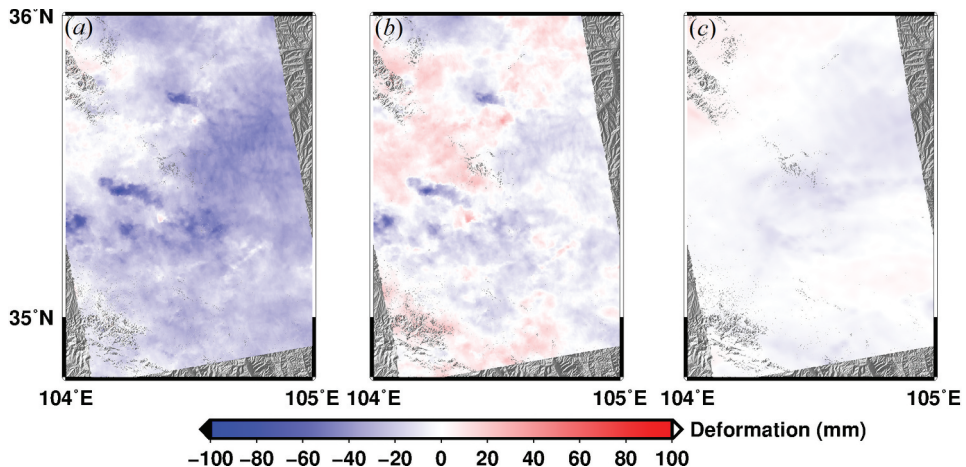


Figure 9. Comparison of uncorrected deformation map with deformation maps corrected with WRF using two different MPs for the dates 6 August and 18 August 2017. (a) Uncorrected, (b) WSM3, (c) M2M.

Considering the reason why M2M predicts a closer ZTD values and can mitigate the atmospheric effect on the InSAR, we perceive that the great regional topographic fluctuation (see Figure 1) between the mountain peak and valley in the study area, results in the uneven temperature and pressure distribution in vertical convective motion and horizontal stratiform. What's more, the different slope and azimuth causes the different time and intensity of solar radiation. A more comprehensive model (i.e., double moment micro-physics scheme) is required to simulate these various processes to predict more accurate atmospheric parameters.

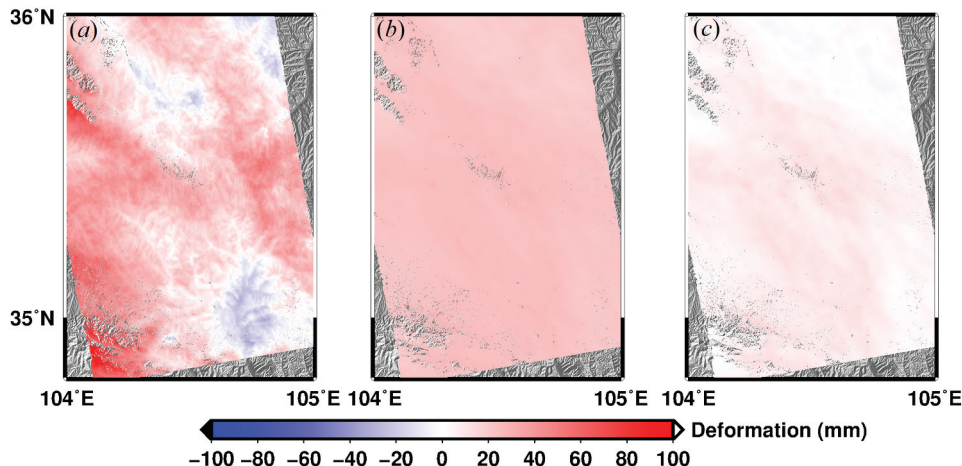


Figure 10. Comparison of uncorrected deformation map with deformation maps corrected with WRF using two different MPs for the dates 14 June and 26 June 2018. (a) Uncorrected, (b) WSM3, (c) M2M.

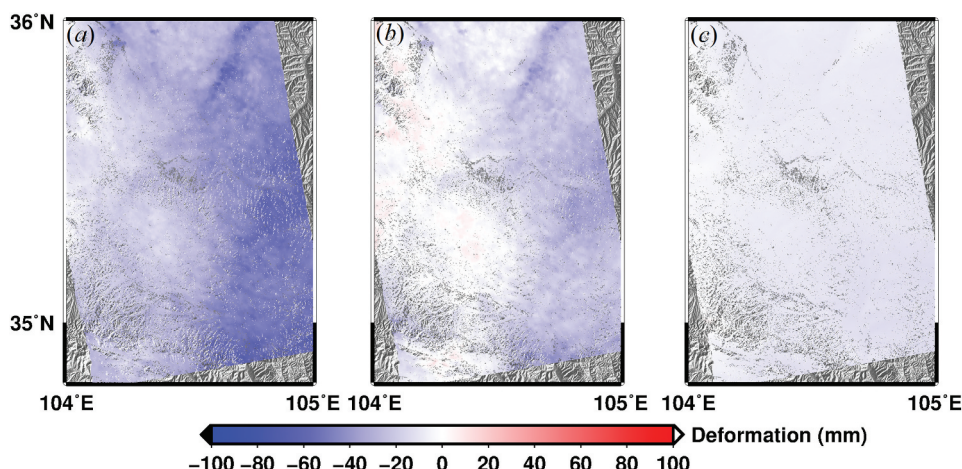


Figure 11. Comparison of uncorrected deformation map with deformation maps corrected with WRF using two different MPs for the dates 1 August and 13 August 2018. (a) Uncorrected, (b) WSM3, (c) M2M.

5. Conclusions

In this research, we first assessed the influence of convective scheme selection (i.e., microphysics schemes) on the ZTD simulation in an effort to obtain more accurate InSAR deformation maps. Four microphysics schemes (WSM3, WSM6, M2M, and WDM6) were utilized in the WRF model to simulate the ZTD for InSAR atmospheric correction over Haiyuan in summer (June, July, and August in the year 2017 and 2018). Sensitivity experiments were conducted under three two-way nested domains with horizontal resolutions of 9 km, 3 km, 1 km. The main conclusions are as follows.



Table 10. Mean, STD and RMS of the deformation maps computed from D-InSAR for the four interferograms with and without WRF-based atmospheric correction.

Date of the interferogram	AC or not	MP	Mean (mm)	STD (mm)	RMS (mm)
7 and 19 June 2017	Uncorrected		-33.0	12.6	35.3
	WRF-based AC	WSM3	-9.3	12.1	12.3
	WRF-based AC	M2M	-3.0	5.2	5.1
6 and 18 August 2017	Uncorrected		-21.0	13.0	25.0
	WRF-based AC	WSM3	-6.9	11.1	11.1
	WRF-based AC	M2M	-1.8	5.2	5.1
14 and 26 June 2018	Uncorrected		15.7	20.4	25.8
	WRF-based AC	WSM3	-1.2	13.5	13.3
	WRF-based AC	M2M	1.6	3.8	3.7
1 and 13 August 2018	Uncorrected		-27.4	16.6	32.0
	WRF-based AC	WSM3	-15.0	11.9	15.5
	WRF-based AC	M2M	-4.5	2.7	4.8

- (1) The absolute ZTD values were simulated and validated with those obtained from four GPS stations. In comparison, the M2M produces the best absolute ZTD values with the smallest mean absolute error (3.3 mm for July in [Figures 3](#) and 6.1 mm for June and August in [Figure 6](#)) of the deviation with the GPS-ZTD values, while the WSM3 scheme generally produces the largest bias with the largest mean absolute error (11.6 mm in [Figure 6](#)). Both WSM3 and WSM6 are less robust than the M2M and WDM6 with respect to the differential values of WRF-ZTD. The Morrison double moment approach, considered to be more comprehensive in representing the stratiform of hydrometeors, is the best choice for simulation of ZTD values over complex topography such as Haiyuan Fault.
- (2) The deformation of D-InSAR without and with WRF-based atmospheric correction notably shows that M2M is the most effective at mitigating atmospheric impact, although all four MPs can mitigate the atmospheric impact to some extent. Based on the [Tables 8](#), [Tables 9](#) and [Tables 10](#), with the WRF-based atmospheric correction using M2M, the MAE, STD and RMS of deformation map are the smallest and closest to 0 mm in the non-deformation area. This result suggests that over complex mountains in summer, it is more suitable to use the M2M microphysics scheme.

The WRF model is robust enough to simulate the atmospheric zenith total delay and it shows potential for eliminating atmospheric impact on D-InSAR application. Although these conclusions are significant, this article is only based on six SAR interferograms cases. More case studies are still needed for different study areas and seasons. Further analysis will be needed if we are to obtain a more robust conclusion regarding the most suitable microphysics schemes for differential ZTD simulation in D-InSAR atmospheric correction. And as an interdisciplinary application, we hope that WRF model can be widely used in the field of remote sensing technology.

Acknowledgements

We are grateful to the reviewers for giving constructive comments. The NCEP GFS-FNL data are available via the NCAR Research Data Archive. The Sentinel-1A SAR images were downloaded

from the European Space Agency, the GPS data used for the zenith total delay (ZTD) validation were downloaded from crustal movement observation network of China (<http://www.neiscn.org/>). We also thank the High-performance Computing Platform of Peking University. We used the Generic Mapping Tools (GMT) software to draw the figures and used GMTSAR to process the SAR images and complement the WRF-based atmospheric correction. We thank LetPub (www letpub.com) for its linguistic assistance during the preparation of this manuscript.

Disclosure statement

No potential conflict of interest was reported by the authors.

Funding

This research was supported by the National Key Research and Development Program of China (No. 2017YFB0502703), Ministry of Science and Technology of the People's Republic of China; and Key Project of Department of Science and Technology of Inner Mongolia Autonomous Region, China

References

- Bekaert, D. P. S., R. J. Walters, T. J. Wright, A. J. Hooper, and D. J. Parker. 2015. "Statistical Comparison of InSAR Tropospheric Correction Techniques." *Remote Sensing of Environment* 170: 40–47. doi:[10.1016/j.rse.2015.08.035](https://doi.org/10.1016/j.rse.2015.08.035).
- Bevis, M., S. Businger, T. A. Herring, C. Rocken, R. A. Anthes, and R. H. Ware. 1992. "GPS Meteorology: Remote Sensing of Atmospheric Water Vapor Using the Global Positioning System." *Journal of Geophysical Research Atmospheres* 97 (D14): 15787–15801. doi:[10.1029/92JD01517](https://doi.org/10.1029/92JD01517).
- Davis, J. L., T. A. Herring, I. I. Shapiro, A. E. E. Rogers, and G. Elgered. 1985. "Geodesy by Radio Interferometry: Effects of Atmospheric Modeling Errors on Estimates of Baseline Length." *Radio Science* 20 (6): 1593–1607. doi:[10.1029/RS020i006p01593](https://doi.org/10.1029/RS020i006p01593).
- Elgered, G., J. L. Davis, T. A. Herring, and I. I. Shapiro. 1991. "Geodesy by Radio Interferometry: Water Vapor Radiometry for Estimation of the Wet Delay." *Journal of Geophysical Research: Solid Earth* 96 (B4): 6541–6555. doi:[10.1029/90JB00834](https://doi.org/10.1029/90JB00834).
- Gong, W., F. J. Meyer, S. Liu, and R. F. Hanssen. 2015. "Temporal Filtering of InSAR Data Using Statistical Parameters from NWP Models." *IEEE Transactions on Geoscience and Remote Sensing* 53 (7): 4033–4044. doi:[10.1109/tgrs.2015.2389143](https://doi.org/10.1109/tgrs.2015.2389143).
- Hanssen Ramon, F. 2001. *Radar Interferometry: Data Interpretation and Error Analysis*. New York: Kluwer Academic Publication.
- Hong, S. and Lim, J. 2006. "The WRF Single-Moment 6-Class Microphysics Scheme (WSM6)." *Journal of the Korean Meteorological Society*, 42, 129–151.
- Hong, S. Y., H. Juang, and Q. Y. Zhao. 1998. "Implementation of Prognostic Cloud Scheme for a Regional Spectral Model. MONTHLY WEATHER REVIEW." *Papers* 126 (10): 2621–2639. doi:[10.1175/1520-0493\(1998\)126<2621:iopcsf>2.0.co;2](https://doi.org/10.1175/1520-0493(1998)126<2621:iopcsf>2.0.co;2).
- Hong, S. Y., J. Dudhia, and S. H. Chen. 2004. "A Revised Approach to Ice Microphysical Processes for the Bulk Parameterization of Clouds and Precipitation." *Monthly Weather Review* 132 (1): 103–120. doi:[10.1175/1520-0493\(2004\)132<0103:ARATIM>2.0.CO;2](https://doi.org/10.1175/1520-0493(2004)132<0103:ARATIM>2.0.CO;2).
- Hu, X., J. Tao, F. Zheng et al. 2014. "Introduction of Physical Process Parameterization Schemes in WRF. GANSU SCIENCE AND TECHNOLOGY." *Papers* 24 (20): 73–75.
- Jankov, I., W. A. Gallus, M. Segal, B. Shaw, and S. E. Koch. 2005. "The Impact of Different WRF Model Physical Parameterizations and Their Interactions on Warm Season MCS Rainfall." *Weather and Forecasting* 20 (6): 1048–1060. doi:[10.1175/WAF888.1](https://doi.org/10.1175/WAF888.1).

- Jung, J., D. Kim, and S. E. Park. 2014. "Correction of Atmospheric Phase Screen in Time Series InSAR Using WRF Model for Monitoring Volcanic Activities." *IEEE Transactions on Geoscience and Remote Sensing* 52 (5): 2678–2689. doi:[10.1109/TGRS.2013.2264532](https://doi.org/10.1109/TGRS.2013.2264532).
- Kan, Y., C. Liu, F. Qiao, Y. Liu, W. Gao, and Z. Sun. 2016. "Effects of Microphysics Parameterization Schemes on the Simulation of a Heavy Rainfall Event in Shanghai." *Proc. SPIE 9975, Remote Sensing and Modeling of Ecosystems for Sustainability XIII*, 99750U. doi: [10.1117/12.2237281](https://doi.org/10.1117/12.2237281).
- Li, Z. H. 2005. "Correction of Atmospheric Water Vapour Effects on Repeat Pass SAR Interferometry Using GPS, MODIS and MERIS Data." PhD diss., University College London.
- Liu, S., R. Hanssen, and A. Mika. 2009. "On the Value of High-Resolution Weather Models for Atmospheric Mitigation in SAR Interferometry." In *IGARSS 2009 International Geoscience and Remote Sensing Symposium*, Cape town, July 12–17.
- Mateus, P., G. Nico, and J. Catalao. 2013a. "Can Spaceborne SAR Interferometry Be Used to Study the Temporal Evolution of PWV?" *Atmospheric Research* 119: 70–80. doi:[10.1016/j.atmosres.2011.10.002](https://doi.org/10.1016/j.atmosres.2011.10.002).
- Mateus, P., G. Nico, and P. M. A. Miranda. 2013b. "Experimental Study on the Atmospheric Delay Based on GPS, SAR Interferometry, and Numerical Weather Model Data." *IEEE Transactions on Geoscience & Remote Sensing* 51 (1): 6–11. doi:[10.1109/TGRS.2012.2200901](https://doi.org/10.1109/TGRS.2012.2200901).
- Mielikainen, J., B. Huang, H. A. Huang, M. Goldberg. 2012. "Improved GPU/CUDA Based Parallel Weather and Research Forecast (WRF) Single Moment 5-Class (WSM5) Cloud Microphysics." *IEEE Journal of Selected Topics in Applied Earth Observations and Remote Sensing: Papers* 5 (4): 1256–1265. doi:[10.1109/jstars.2012.2188780](https://doi.org/10.1109/jstars.2012.2188780).
- Morrison, H., G. Thompson, and V. Tatarkii. 2009. "Impact of Cloud Microphysics on the Development of Trailing Stratiform Precipitation in a Simulated Squall Line: Comparison of One- and Two-Moment Schemes." *Monthly Weather Review* 137 (3): 991–1007. doi:[10.1175/2008MWR2556.1](https://doi.org/10.1175/2008MWR2556.1).
- National Centers for Environmental Prediction/National Weather Service/NOAA/U.S. Department of Commerce. 2015. "NCEP GFS 0.25 Degree Global Forecast Grids Historical Archive." *Research Data Archive at the National Center for Atmospheric Research, Computational and Information Systems Laboratory*. doi:[10.5065/D65D8PWK](https://doi.org/10.5065/D65D8PWK). Accessed on 22 Jan. 2021.
- Nico, G., R. Tome, J. Catalao, and P. M. A. Miranda. 2011. "On the Use of the Wrf Model to Mitigate Tropospheric Phase Delay Effects in Sar Interferograms." *IEEE Transactions on Geoscience & Remote Sensing* 49 (12): 4970–4976. doi:[10.1109/TGRS.2011.2157511](https://doi.org/10.1109/TGRS.2011.2157511).
- Shi, J. L. 2013. *Research on Different Rainfall Simulation of WRF Model with Various Parameterization Schemes in Inner Mongolia*. Nanjing: Nanjing.
- Skamarock, W. C., J. B. Klemp, J. Dudhia, D. O. Gill, D. M. Barker, M. G. Duda, X. Huang, W. Wang, J. G. Powers. 2008. "A Description of the Advanced Research WRF Version 3." *NCAR Tech. Note NCAR/TN-475+STR*, 113. doi:[10.5065/D68S4MVH](https://doi.org/10.5065/D68S4MVH)
- Yun, Y. 2015. "Mitigating Atmospheric Effects in Repeat-Pass Space-borne InSAR Measurement through Data Assimilation and Numerical Simulations with WRF Model." PhD diss., Peking University.
- Yun, Y., Q. Zeng, B., W. Green, and F. Zhang. 2015. "Mitigating Atmospheric Effects in InSAR Measurements through High-resolution Data Assimilation and Numerical Simulations with a Weather Prediction Model." *International Journal of Remote Sensing* 36 (8): 2129–2147. doi:[10.1080/01430061.2015.1034894](https://doi.org/10.1080/01430061.2015.1034894).